The Astrophysical Journal, 659:1496–1504, 2007 April 20

IRREGULAR SINGULARITY OF THE MAGNETOROTATIONAL INSTABILITY IN A KEPLERIAN DISK

M. Furukawa, Z. Yoshida, and M. Hirota
Graduate School of Frontier Sciences, The University of Tokyo, Kashiwa, Chiba 277-8561, Japan;
furukawa@k.u-tokyo.ac.jp

and

V. Krishan
Indian Institute of Astrophysics, Bangalore 560 034, India
Received 2006 May 12; accepted 2007 January 12

ABSTRACT

The center of a Keplerian disk is an irregular singularity for the eigenfunctions of magnetorotational instabilities. The system is studied using the small-radius approximation, which by no means implies that the analysis is valid only in the vicinity of the center of the astrophysical disks. In fact, the singularity has an effect on the entire disk and yields continuous eigenvalues (growth rates in the unstable regime and real frequencies in the stable regime) with rather intriguing implications for the non-Hermitian nature of the rotating plasmas. Through the Laplace transform, as well as numerical simulations, interesting long-term behavior of the instability has been found.

Subject headings: accretion, accretion disks — instabilities — plasmas

1. INTRODUCTION

The magnetorotational instability (MRI; Velikhov 1959; Chandrasekhar 1960) in accretion disks (Balbus & Hawley 1998) is considered as the driving mechanism of turbulence that can bring about anomalous angular momentum transport (Balbus & Hawley 1991). In Balbus & Hawley (1991), the dispersion relation of the MRI was studied by "local analysis," assuming sinusoidal waves in both the radial and the height directions of the accretion disk. Taking into account the inhomogeneity of the equilibrium in the radial direction, Dubrulle & Knobloch (1993) and Curry et al. (1994) studied the radial mode structure by solving a second-order differential equation. While the eigenvalue problem looks rather standard (especially for the axisymmetric modes, the determining equation can be cast into the form of the Schrödinger equation), some mathematical difficulties are hidden under the superficial appearance of the simple form.

First of all, we remark that the waves and instabilities in a rotating disk obey a non-Hermitian evolution equation, and hence, the standard method of normal-mode analysis does not apply. The eigenvalue problem, derived by replacing $\partial/\partial t$ by $-i\omega$, may give only some particular solutions to the evolution equation. However, the general solution may not be given by the linear combination (sum or integral over the whole spectra) of these eigenmodes. Each eigenmode is not independent of (orthogonal to) the others, and the set of eigenmodes may fall short or exceed to span the whole space.

The eigenvalue problem becomes more difficult when an essential singularity occurs, which represents a compound of an infinite number of "coupled (nonorthogonal)" degrees of freedom. Indeed, this is the case when we consider a Keplerian disk (or, more generally, if we assume a rotation frequency that decreases faster than the inverse of the radius)—the center of the disk turns out to be an "irregular singularity" (S. M. Mahajan 2006, private communication). Of course, the radius $R = 0$ is a mathematical artifact. We have to consider a finite-radius inner boundary for the idealized model of the disk dynamics. However, the existence of a singularity at $R = 0$ implies that the radial structures of the modes are highly sensitive to the boundary condition to be imposed near the axis. Therefore, we are motivated to analyze the effect of the singularity to understand the structure of modes near $R = 0$.

In this paper we will show that the irregular singularity generates a continuum of eigenvalues (point spectra). The corresponding eigenmodes have finite energy (square integrable), while their spatial frequency is infinite in the vicinity of $R = 0$. The uncountable potency of the eigenmodes does not contradict the property of the countable degrees of freedom of the Hilbert space, because the orthogonality of the eigenmodes is broken by the non-Hermitian property of the system.

As mentioned above, we have to carefully interpret the results of the eigenvalue problem. By studying the initial-value problem (invoking the Laplace transform, as well as numerical simulation), we will reveal the physical implication of the continuum of the eigenvalues. The radial structure of the instability continues to change slowly for an appreciably long time.

This paper is organized as follows. In § 2 we derive the basic equation of our analysis on the basis of incompressible magnetohydrodynamics (MHD). Several properties of the system, such as its non-Hermitian nature, the reality of the eigenvalues, and the existence of the irregular singular point, are described. The corresponding eigenvalue problem is solved in § 3. We find the continuum of real eigenvalues. The time evolution of such a system is analyzed in § 4 via the Laplace transform. We find that the spatial structure of the linearly growing wave continues to change slowly for a significantly long time due to the densely populated poles of the growing solution. Section 5 describes the numerical results of both eigenvalue and initial-value approaches, which agree well with the analytical results. Concluding remarks are given in § 6.

2. BASIC EQUATIONS

In this study, we start from the incompressible version of the linearized magnetohydrodynamic equations including equilibrium plasma flow (Frieman & Rotenberg 1960),

$$\rho\frac{\partial^2 x}{\partial t^2}+2\rho\boldsymbol{v}\cdot\nabla\frac{\partial x}{\partial t}=\left(\nabla\times\tilde{\boldsymbol{B}}\right)\times\boldsymbol{B}+(\nabla\times\boldsymbol{B})\times\tilde{\boldsymbol{B}} - \nabla\tilde{p}+x\cdot\nabla(\rho\boldsymbol{v}\cdot\nabla\boldsymbol{v})-\rho\boldsymbol{v}\cdot\nabla(\boldsymbol{v}\cdot\nabla x), \quad (1)$$

$$\nabla\cdot x=0, \quad (2)$$

where ρ is the mass density, $\boldsymbol{v}$ and $\boldsymbol{B}$ are the equilibrium velocity and magnetic field, respectively, x and $\tilde{p}$ are the plasma displacement and the perturbed pressure, respectively, and $\tilde{\boldsymbol{B}}$ is the perturbed magnetic field defined by

$$\tilde{\boldsymbol{B}}=\nabla\times(x\times\boldsymbol{B}). \quad (3)$$

These variables are normalized by their typical values, such as the magnetic field B_0, the mass density ρ_0, and the Alfvén time $\tau_{\rm A}=R_0/v_{\rm A}$ with $v_{\rm A}=B_0/(\mu_0\rho_0)^{1/2}$. The pressure is normalized by the magnetic pressure. It is noted that we assume the plasma rotation is Keplerian ($\Omega^2=GM/R^3$) in this paper, where G is the gravitational constant and M is the mass of the central object. If we normalize the representation of the Keplerian rotation by using a scale length R_0, we obtain $\Omega=R^{-3}$ with $\tau_{\rm A}^2GM/R_0^3=GM/v_{\rm A}^2R_0=1$. This relationship determines the scale length R_0 as

$$R_0=GM/v_{\rm A}^2. \quad (4)$$

Figure 1 shows the contour plot of R_0 in meters. The mass of the Sun is about 2×10^{30} kg and the diameter of the largest accretion disk detected to date is about 2×10^4 AU or 3×10^{15} m (Chini et al. 2004). For a considerably wide range of parameters, the scale length R_0 may be much greater than the size of the accretion disks. Assuming a Sun-like star of 1 $M_\odot$, the approximation $R\ll1$, or $R\ll R_0$ in the physical dimension, which will be used in the following analysis, does not necessarily mean that we concentrate only on the region very near to the massive central object.

As the simplest equilibrium in which MRI can occur, we assume the constant mass density $\rho=1$, the constant magnetic field $\boldsymbol{B}=B\hat{\boldsymbol{Z}}$ with $B=1$, and the equilibrium velocity $\boldsymbol{v}=R\Omega(R)\hat{\boldsymbol{\theta}}$. The self-gravity is neglected. Here $\Omega(R)$ is the angular rotation frequency normalized by using the Alfvén time, (R,θ,Z) are the cylindrical coordinates, and $\hat{\boldsymbol{\theta}}$ and $\hat{\boldsymbol{Z}}$ are the unit vectors. The Alfvén velocity in the normalized variables is unity. If we assume the axisymmetry of the perturbation x, $\tilde{p}$, and $\tilde{\boldsymbol{B}}$ and apply the Fourier representation in the vertical direction as $\exp(ikZ)$, we obtain the evolution equation

$$\left(i\frac{\partial}{\partial t}\right)^2\begin{pmatrix}L_1 & I\\ L_2 & 0\end{pmatrix}\begin{pmatrix}\xi_R\\ \zeta_R\end{pmatrix}=\omega_{\rm A}^2\begin{pmatrix}-L_0 & 0\\ 0 & I\end{pmatrix}\begin{pmatrix}\xi_R\\ \zeta_R\end{pmatrix}, \quad (5)$$

where ξ_R is the radial component of the plasma displacement, the definition of ζ_R is given by the bottom half of equation (5), $\omega_{\rm A}=k$ is the normalized Alfvén frequency, k is the wavenumber normalized by the system size, and the operators L_j ($j=0,1,2$) are defined by

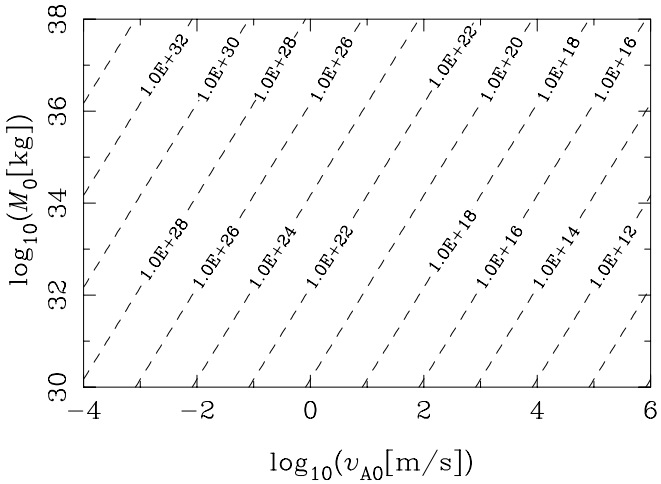

FIG. 1.—Contour plot of the typical scale length R_0 (in meters) given in eq. (4). For a considerably wide range of parameters, R_0 is much greater than the size of the accretion disks.

$$L_2=\frac{\partial}{\partial R}\left(\frac{1}{R}\frac{\partial}{\partial R}R\right)-k^2, \quad (6)$$

$$L_1=-2\frac{\partial}{\partial R}\left(\frac{1}{R}\frac{\partial}{\partial R}R\right)+k^2\left[2+\frac{R(\Omega^2)'+4\Omega^2}{\omega_{\rm A}^2}\right], \quad (7)$$

$$L_0=\frac{\partial}{\partial R}\left(\frac{1}{R}\frac{\partial}{\partial R}R\right)-k^2\left[1+\frac{R(\Omega^2)'}{\omega_{\rm A}^2}\right]. \quad (8)$$

The boundary conditions are $\xi_R=0$ at $R=0$ and $R=R_a\neq0$, where R_a denotes an outer boundary. The matrix operator on the right-hand side of equation (5) is Hermitian with a boundary condition $\xi_R=0$ at the boundaries. However, the matrix operator on the left-hand side is non-Hermitian. Multiplying the inverse of the matrix operator on the left-hand side, we see that the time evolution of the variables ξ_R and ζ_R is governed by a non-Hermitian operator. It is known that systems governed by non-Hermitian operators exhibit varieties of interesting phenomena such as nonexponential growth of instabilities (Tatsuno et al. 2001; Furukawa & Tokuda 2005; Hirota et al. 2005). In addition to such transient phenomena, several interesting properties are found via the eigenvalue approach. Thus, we analyze the eigenvalue problem in § 3.

3. IRREGULAR SINGULARITY AND CONTINUUM OF REAL EIGENVALUES

Adopting the Fourier representation in time $\exp(-i\omega t)$ in equation (5), the eigenvalue ω^2 can be generally complex, since the eigenvalue problem is characterized by the non-Hermitian operator. The coupled equations are summarized as

$$\frac{\partial}{\partial R}\left[\frac{1}{R}\frac{\partial}{\partial R}(R\xi_R)\right]-k^2\left[1-\frac{R(\Omega^2)'}{\omega^2-\omega_{\rm A}^2}-\frac{4\omega^2\Omega^2}{(\omega^2-\omega_{\rm A}^2)^2}\right]\xi_R=0, \quad (9)$$

where the prime denotes the radial derivative. If we assume that the radial derivative is negligible, the local dispersion relation of the classical MRI is recovered as

$$\omega^2=\omega_{\rm A}^2+\Omega(2\Omega+R\Omega')\pm\Omega\sqrt{4\omega_{\rm A}^2+(2\Omega+R\Omega')^2}. \quad (10)$$

Multiplying equation (9) by $(\omega^2-\omega_{\rm A}^2)^2 R\xi_R^*$, where ξ_R^* is the complex conjugate, and integrating over R in an appropriate domain, we obtain

$$\omega^2=\frac{-(2\omega_{\rm A}^2 a+b+c)\pm\sqrt{(b+c)^2+4\omega_{\rm A}^2 ac}}{-2a}, \tag{11}$$

where a, b, and c are defined by

$$a=\int dR\left[\frac{1}{R}\left|\frac{\partial(R\xi_R)}{\partial R}\right|^2+k^2R|\xi_R|^2\right], \tag{12}$$

$$b=k^2\int dR\,R^2(\Omega^2)'|\xi_R|^2, \tag{13}$$

$$c=4k^2\int dR\,R\Omega^2|\xi_R|^2. \tag{14}$$

We see that a and c are positive; thus, ω^2 becomes always real. Therefore, this eigenvalue problem is a special class among non-Hermitian systems in which ω^2 can be generally complex.

By introducing $\varphi=R^{1/2}\xi_R$, equation (9) can be rewritten in a form of the Schrödinger equation as

$$\frac{d^2\varphi}{dR^2}-V(R;\omega^2)\varphi=0, \tag{15}$$

where if the equilibrium rotation is Keplerian ($\Omega^2=R^{-3}$), the potential V is given by

$$V=\frac{3}{4}R^{-2}+k^2\left[1-\frac{\omega^2+3\omega_{\rm A}^2}{(\omega^2-\omega_{\rm A}^2)^2}R^{-3}\right], \tag{16}$$

which diverges as R^{-3} near the center. We see that $R=0$ is an irregular singular point. It is noted that this is written in a form of the Schrödinger equation. However, we need to be careful since the "potential" V includes the eigenvalue ω^2 as given above. Thus, we should interpret this equation as $d^2\varphi/dR^2-V(R;\omega^2)\varphi=E\varphi$ with $E=0$, i.e., we try to find a wave with zero energy ($E=0$) in a potential V which changes its shape if ω^2 is changed. It may also be worth pointing out that two values of ω^2 give the same potential V. For example, if $(\omega^2+3\omega_{\rm A}^2)/(\omega^2-\omega_{\rm A}^2)^2=1/A=$ const, then $\omega^2=\omega_{\rm A}^2+A/2\pm\frac{1}{2}[A(A+16\omega_{\rm A}^2)]^{1/2}$. When a constant A gives a pair of positive and negative ω^2, the stable and unstable eigenmodes share the mode structure.

In order to investigate the behavior of the eigenmode around the massive central object, we approximate the potential in equation (16) for $R\ll 1$. Then the R^{-3} term becomes dominant, and the eigenvalue problem can be written as

$$R^3\frac{d^2\varphi}{dR^2}+\lambda\varphi=0, \tag{17}$$

where λ is given by

$$\lambda=k^2\frac{\omega^2+3\omega_{\rm A}^2}{(\omega^2-\omega_{\rm A}^2)^2}=\text{const}. \tag{18}$$

This is similar to an equation of motion of a pendulum with variable mass: $m(t)\ddot{x}(t)+\lambda x(t)=0$ with positive λ. If $m(t)\ll 1$ when $t\ll 1$ and $m(t)$ increases in time, the oscillation is rapid at the beginning and it becomes slower in time. Then we expect

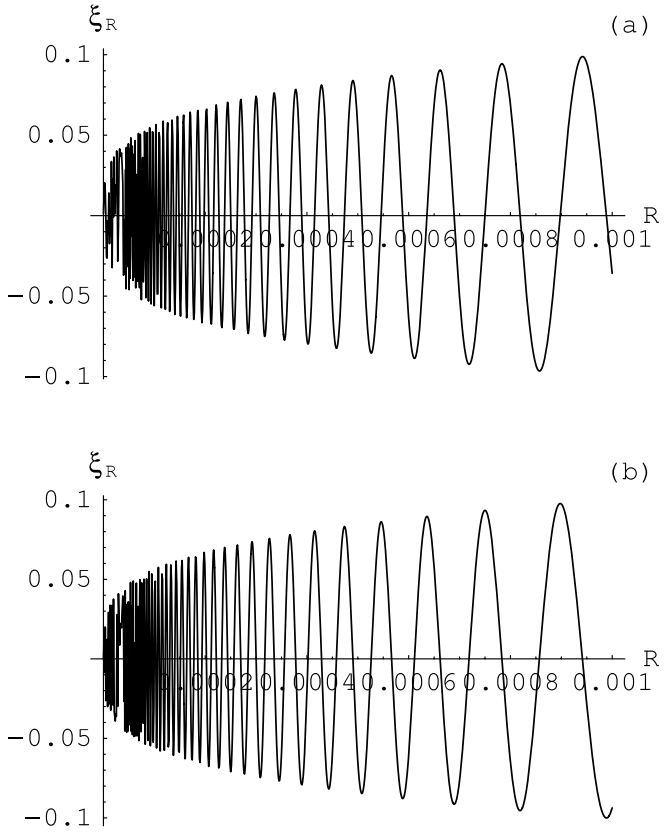

FIG. 2.—Eigenfunctions $\xi_R=R^{-1/2}\varphi$ given in eq. (19) for $\lambda=1$. (*a*) $J_1(2(\lambda/R)^{1/2})$; (*b*) $Y_1(2(\lambda/R)^{1/2})$. Both of them satisfy the boundary condition $\xi_R=0$ at $R=0$. The radial variation is rapid around $R=0$, and it becomes slower as R increases.

that equation (17) with positive λ gives oscillatory solutions for which radial variation is rapid around $R=0$, and it becomes slower as R increases. Transforming the coordinate as $x=R^{-1/2}$, we find the solution of equation (17) analytically for $\lambda>0$ as

$$\varphi=c_1R^{1/2}J_1\left(2(\lambda/R)^{1/2}\right)+c_2R^{1/2}Y_1\left(2(\lambda/R)^{1/2}\right), \tag{19}$$

where J_1 and Y_1 are the Bessel functions of the first order. Figure 2 shows the eigenfunctions $\xi_R=R^{-1/2}\varphi$ for $\lambda=1$. We see that the radial variation around the origin is quite rapid and it becomes slower as R increases. This kind of solution cannot be approximated by the "local" dispersion relation where the radial variation is neglected. It is noted that the radial variation is so rapid that the numerical resolution is not enough in the plotting software. The important point is that these two independent solutions both go to zero as they approach $R=0$ for continuous values of positive λ, i.e., continuous values of $\omega^2>-3\omega_{\rm A}^2$. It is noted that these eigenfunctions are square integrable as

$$\int_0^{R_a}dR\,R|\xi_R|^2=2\int_{R_a^{-1/2}}^{\infty}dx\,x^{-5}\left|c_1J_1\left(2\sqrt{\lambda}x\right)+c_2Y_1\left(2\sqrt{\lambda}x\right)\right|^2, \tag{20}$$

where R_a denotes an outer boundary. In Hermitian systems, on the other hand, such a continuum appears only at the stable side $\omega^2>0$ with singular (non–square-integrable) eigenfunctions.

For $\lambda < 0$ or $\omega^2 < -3\omega_A^2$, J_1 and Y_1 in equation (19) are changed to the modified Bessel functions I_1 and K_1. Then the boundary conditions cannot be satisfied, and no eigenvalue exists.

The reason why we obtain such a continuum of eigenvalues is because the transformation of the coordinate $x = R^{-1/2}$ maps a finite domain in R to a semi-infinite domain in x. This is similar to the spectrum of the one-dimensional Laplacian operator (e.g., d^2/dx^2); in an infinite domain it is continuous (Fourier transform), on the other hand, it is discrete in a finite domain (Fourier expansion). This coordinate transformation works well only when $R = 0$ is an irregular singular point. Therefore, the non-Hermitian property and the irregular singular point generate the continuum of eigenvalues with square-integrable eigenfunctions even at the unstable side $\omega^2 < 0$. It is noted that such a continuum of eigenvalues with square-integrable eigenfunctions can be obtained for more general rotation-frequency profiles $\Omega^2 = R^p$ with $p < -2$ (see the Appendix).

The number of eigenfunctions is uncountably infinite, which is too much to decompose a perturbation or a regular function. Also, the eigenfunctions are not orthogonal with each other.

Finally, we discuss the relationship between the instability found in this section and the classical MRI. First of all, the local dispersion relation of the classical MRI is derived by neglecting the radial derivative of ξ_R as mentioned below equation (9). Thus, if the radial derivative of the global eigenfunctions can be small enough to be neglected, the eigenvalues can be approximated by the local dispersion relation. However, the global modes found in this section are always constructed by balancing the radial derivative term with the potential term, and the eigenfunctions oscillate rapidly in R especially around $R = 0$. Therefore, the local dispersion relation cannot approximate our global instabilities. Furthermore, the maximum growth rate, $\sqrt{3}\omega_A = \sqrt{3}k$, becomes larger for larger k, which is different from the classical MRI; the classical MRI is stabilized for large k because of the magnetic tension. However, in our analysis, we have a region where the plasma rotation shear can be large enough to destabilize the MRI even for such large k. Of course, if k becomes too large, we have to include higher order derivative terms, such as viscosity, which has not been taken into account in the present study. Then there will be a limiting k value above which our analysis is not valid. It is also noted that the maximum growth rate looks independent of the plasma rotation frequency, however, it is not true; it comes from the plasma rotation frequency profile Ω. For the general rotation profile, $\Omega^2 = R^p$ with $p < -2$, the parameter λ is modified as (see the Appendix)

$$\lambda_p = k^2 \frac{(p+4)\omega^2 - p\omega_A^2}{(\omega^2 - \omega_A^2)^2}, \tag{21}$$

and therefore, we find the continuum at $\omega^2 > [p/(p+4)]\omega_A^2$ for $-4 < p < -2$. Thus, the maximum growth rate becomes $[-p/(p+4)]^{1/2}\omega_A$. For the Keplerian rotation $p = -3$, $\sqrt{3}\omega_A$ is recovered. It is noted that the growth rate (frequency) in our paper is normalized by the Alfvén frequency (see the text below eq. [3]). It is important to note that the global instabilities in the present paper cannot be found if we impose the boundary condition artificially at finite R. If we change the location of the artificial boundary, the growth rate and the eigenfunctions change. Also, the local dispersion relation of the classical MRI is not a limiting case of our global instabilities. However, the origin of the instability is the same as the classical MRI.

4. TIME EVOLUTION OF MRI

In the following we study the time evolution for the case of the Keplerian rotation by solving the initial-value problem via the Laplace transform. For $R \ll 1$, the evolution equation becomes

$$\frac{\partial^4}{\partial t^4}\left(R^3\frac{\partial^2\varphi}{\partial R^2}\right) - \frac{\partial^2}{\partial t^2}\left(-2\omega_A^2 R^3\frac{\partial^2\varphi}{\partial R^2} + k^2\varphi\right) + \omega_A^2\left(\omega_A^2 R^3\frac{\partial^2\varphi}{\partial R^2} + 3k^2\varphi\right) = 0. \tag{22}$$

Defining the Laplace transform of $\varphi(R, t)$ as

$$\Phi(R, \omega) = \int_0^\infty dt\, e^{i\omega t}\varphi(R, t), \tag{23}$$

we obtain

$$R^3\frac{\partial^2\Phi}{\partial R^2} + \lambda\Phi = \frac{i\omega}{(\omega^2 - \omega_A^2)^2}R^3 f(R, 0), \tag{24}$$

where $f(R, 0) = \partial^2[\partial^2\varphi(R, 0)/\partial t^2]/\partial R^2$ is only retained as an initial condition for simplicity and $\lambda = k^2(\omega^2 + 3\omega_A^2)/(\omega^2 - \omega_A^2)^2$.

The homogeneous solution to equation (24) is exactly the same as found for equation (19), $\Phi(R, \omega) = c_1\Phi_J + c_2\Phi_Y$, where Φ_J and Φ_Y are given by $\Phi_J = R^{1/2}J_1(2(\lambda/R)^{1/2})$ and $\Phi_Y = R^{1/2}Y_1(2(\lambda/R)^{1/2})$, respectively. By using the variation of parameters, we obtain the following equation for determining $c_1(R)$ and $c_2(R)$:

$$\begin{pmatrix} \Phi_J & \Phi_Y \\ \dfrac{\partial\Phi_J}{\partial R} & \dfrac{\partial\Phi_Y}{\partial R} \end{pmatrix}\begin{pmatrix} c_1'(R) \\ c_2'(R) \end{pmatrix} = \begin{pmatrix} 0 \\ \dfrac{i\omega}{(\omega^2 - \omega_A^2)^2}f(R, 0) \end{pmatrix}. \tag{25}$$

Integration of these equations requires two boundary conditions for the determination of the two integration constants $\bar{c}_1$ and $\bar{c}_2$. The first boundary condition is $\Phi(0, \omega) = 0$, which is satisfied trivially, since Φ_J and Φ_Y both go to zero at $R = 0$. The second boundary condition, $\Phi(R_a, \omega) = 0$, can only give the relationship between $\bar{c}_1$ and $\bar{c}_2$. Then we obtain

$$\Phi = \frac{-\pi i\omega}{(\omega^2 - \omega_A^2)^2}\left(\int_0^R \{dR' f(R')[\Phi_J(R', \omega)\Phi_Y(R, \omega) - \Phi_Y(R', \omega)\Phi_J(R, \omega)]\} + \frac{\Phi_Y(R, \omega)}{\Phi_Y(R_a, \omega)}\int_0^{R_a}\{dR' f(R') \times [\Phi_J(R_a, \omega)\Phi_Y(R', \omega) - \Phi_Y(R_a, \omega)\Phi_J(R', \omega)]\} + \bar{c}_1\left[\Phi_J(R, \omega) - \frac{\Phi_J(R_a, \omega)}{\Phi_Y(R_a, \omega)}\Phi_Y(R, \omega)\right]\right). \tag{26}$$

The inverse Laplace transform of Φ gives the time evolution; we have to analyze the poles of Φ in the complex ω-plane. In the following we take $\bar{c}_1 = 0$, since the $\bar{c}_1$ term does not include the initial condition. If we allow this term to remain, a perturbation can arise even for zero initial condition $f(R, 0) = 0$, which never occurs physically. This choice reduces the number of eigenfunctions from uncountably infinite to countably infinite.

By using the asymptotic form of the Bessel functions for $2(\lambda/R)^{1/2} \gg 1$, we find that poles of infinite order exist at $\omega = \pm k$. In addition, we also find poles at ω satisfying $\Phi_Y(R_a, \omega) = 0$.

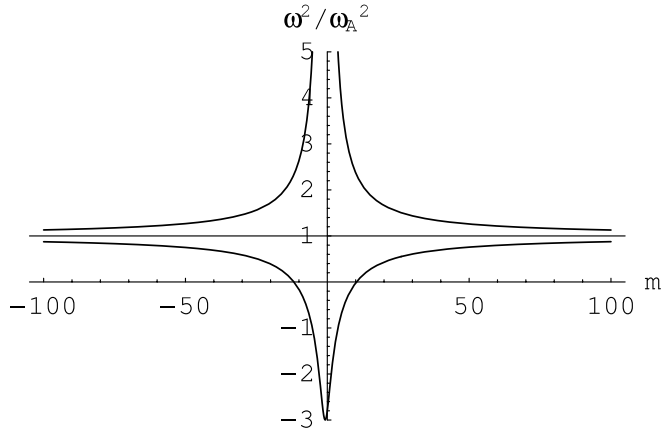

FIG. 3.—Poles ω^2 as a function of m. Note that m is an integer, but it is shown here as a continuous variable.

If we assume $2(\lambda/R)^{1/2} \gg 1$ again, Φ_Y can be represented by a sinusoidal function, and we obtain the poles at ω satisfying

$$2\sqrt{\frac{\lambda}{R_a}} - \frac{3}{4}\pi = m\pi, \tag{27}$$

where m is an integer and λ is a function of ω^2. Figure 3 shows ω^2 obtained by solving the above equation. Note that although m is an integer, it is treated as a continuous variable in the plots. We see that there are a lot of poles at the unstable side $\omega^2 < 0$. In the parameters used in Figure 3, $R_a = 0.01$ (or $R_a = 0.01R_0$ in the physical dimension) and $k = 1$, we find more than 20 poles at $\omega^2 < 0$. The minimum value of ω^2 is approximately $-3\omega_A^2$ for which $m = -1$, which means the maximum growth rate is approximately $\sqrt{3}\omega_A$. We also see that ω^2 diverges at $m = -\frac{3}{4}$ if m is continuous; however, m cannot be $-\frac{3}{4}$, and therefore, ω^2 is bounded. For large m, ω^2 approaches ω_A^2, which means $\omega = \pm\omega_A$ are accumulation points.

Let us estimate the spacing among the poles around $\omega^2 = -3\omega_A^2$. If they are densely distributed, the most unstable mode needs a significantly long time to dominate the others. This means that the initial condition can affect the following time evolution for a long time. The poles originates from the nodes of $\Phi_Y(2(\lambda/R_a)^{1/2})$. Thus, the poles can be represented as

$$\omega^2 = \omega_A^2 + \frac{2k^2}{R_a r_j^2} \pm \sqrt{\frac{4k^2}{R_a r_j^2}\left(4\omega_A^2 + \frac{k^2}{R_a r_j^2}\right)}, \tag{28}$$

where r_j are the nodes of the Bessel function Y_1. Figure 4 schematically shows the poles in the complex ω-plane. The minus sign in equation (28) can yield poles at the unstable side $\omega^2 < 0$. We see that the maximum growth rate is approximately $\sqrt{3}\omega_A$ for the smallest node $r_1 \simeq 2.2$. As j increases, $|\mathrm{Im}\,\omega|$ decreases and passes the origin, and ω becomes pure real. Then they eventually accumulate to $\omega = \pm\omega_A$. This accumulation of the point spectra to the edge of the Alfvén continuum is known in MHD systems (Bondeson et al. 1987; Keppens et al. 2002). The plus sign in equation (28) always gives positive ω^2. For the smallest node r_1, $|\mathrm{Re}\,\omega|$ is huge, which is not plotted in Figure 4. As j increases, $|\mathrm{Re}\,\omega|$ decreases and eventually accumulates to $\omega = \pm\omega_A$.

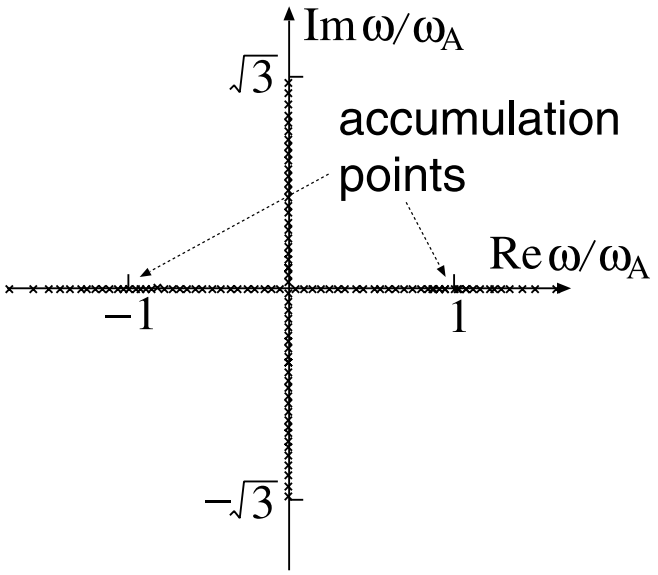

FIG. 4.—Schematic picture of the poles in the complex ω-plane. The countably infinite number of poles exist, and the maximum growth rate is approximately $\sqrt{3}\omega_A$. They accumulate to $\omega = \pm\omega_A$.

When $R_a \ll 1$, we obtain

$$\omega_1^2 - \omega_2^2 = 2k^2 R_a\left(r_1^2 - r_2^2\right), \tag{29}$$

where ω_1 and ω_2 are poles related to the nodes r_1 and r_2, respectively. Therefore, the mode with ω_1 cannot dominate the others for a long time when k is small.

For example, $k = 1$ and $R_a = 0.01$ gives $\omega_1^2 = -2.8231\omega_A^2$ and $\omega_2^2 = -2.2364\omega_A^2$. Thus, the difference between the maximum growth rate and the second is about $0.18\omega_A$, which means that the most unstable mode dominates the others after several tens of Alfvén time. On the other hand, for $k = 0.01$, $\omega_1^2 = -2.8231 \times 10^{-4}\omega_A^2$ and $\omega_2^2 = -2.2364 \times 10^{-4}\omega_A^2$. Thus, the difference between the maximum growth rate and the second one is about $1.8 \times 10^{-3}\omega_A$, and the most unstable mode dominates the others after more than 10^3 Alfvén time.

5. NUMERICAL RESULTS

We have solved the eigenvalue problem in equation (15) numerically. It is noted that the approximation $R \ll 1$ is not used in solving it numerically. The computational domain was chosen as $R \ll 1$. Actually, it was chosen as $R = 0$ to $R = R_a = 0.01$. The boundary condition is set as $\varphi = 0$ at $R = 0$ and $R = R_a$. The wavenumber was chosen as $k = 1$.

Figure 5 shows the eigenfunctions related to (Fig. 5*a*) the first through the fifth smallest and (Fig. 5*b*) the 11th through the 15th smallest eigenvalues. The eigenfunctions are normalized by their norms. We see rapid oscillations of φ near the origin, especially in Figure 5*b*. The eigenvalues are expected to be continuous from the preceding analysis; however, the discretization procedure for the numerical treatment makes the eigenvalues discrete. The values of the first and the 15th smallest eigenvalues are $\omega^2 = -2.9997\omega_A^2$ and $-2.8024\omega_A^2$, respectively. These values approach $\omega^2 = -3\omega_A^2$ if we increase the number of grid points, which may numerically indicate the existence of the continuum of eigenvalues. In Figure 5 we took 1000 grid points in R; however, the resolution is not enough to capture the rapid oscillations near the origin. It is impossible to capture them correctly by the numerical scheme, since the analytic solution shows that the oscillation of φ becomes infinitely rapid near the origin.

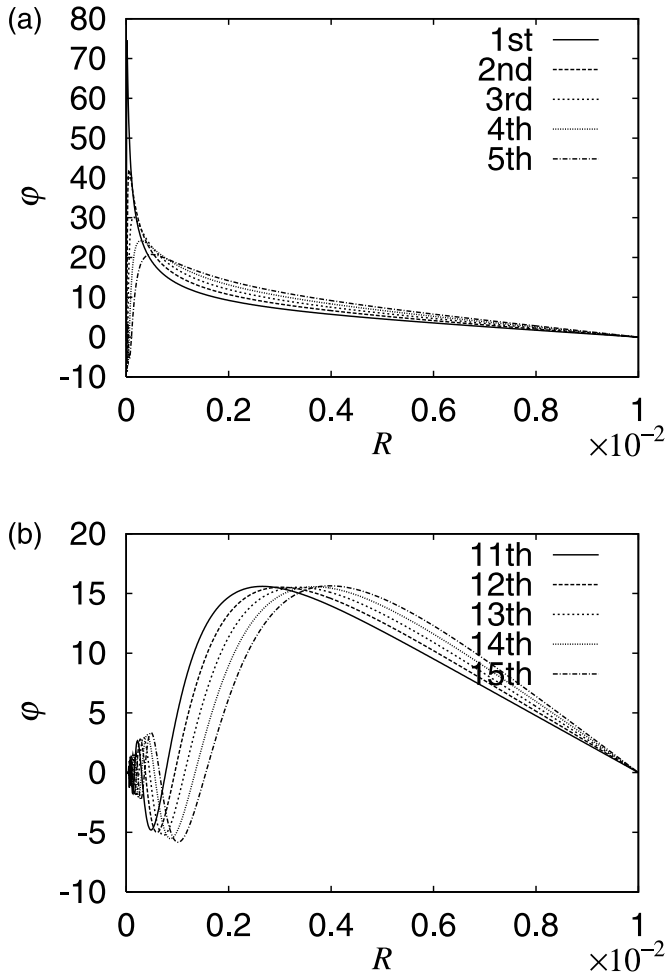

FIG. 5.—Numerically obtained eigenfunctions. (*a*) Eigenfunctions related to the first through the fifth smallest eigenvalues. (*b*) Eigenfunctions related to the 11th through the 15th smallest eigenvalues. Rapid oscillations near the origin are seen.

As a reference, we also calculated the eigenvalues and eigenfunctions for the rotation profile

$$\Omega^2 = (R^2 + \varepsilon^2)^{-3/2}, \tag{30}$$

where ε is a small parameter. Then this profile does not diverge at the origin and approaches the Keplerian rotation as ε goes to zero. Figure 6 shows the first to the fourth smallest eigenvalues as functions of $\sqrt{\varepsilon}$. We see that the eigenvalues approach the values for the Keplerian rotation $\varepsilon = 0$ as ε is decreased. It is noted that the numerically obtained ω^2 for $\varepsilon = 0$ is slightly different from the values by equation (28). This is because equation (28) is derived by assuming the potential V in equation (16) by the R^{-3} term only; however, the R^{-2} term can be comparable even for

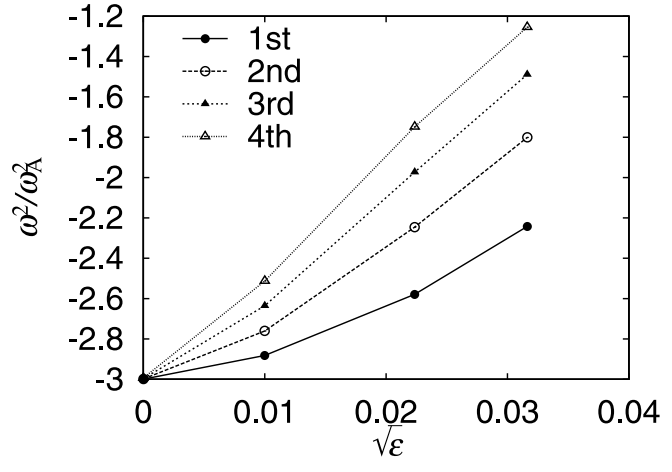

FIG. 6.—First to fourth smallest eigenvalues as functions of $\sqrt{\varepsilon}$. The eigenvalues approach the values for the Keplerian rotation $\varepsilon = 0$ as ε is decreased.

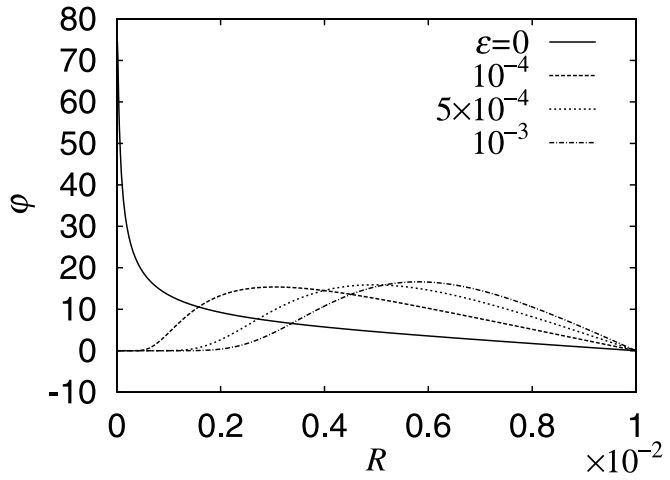

FIG. 7.—Eigenfunction corresponding to the smallest eigenvalue is shown as a function of ε. They are normalized by their norms.

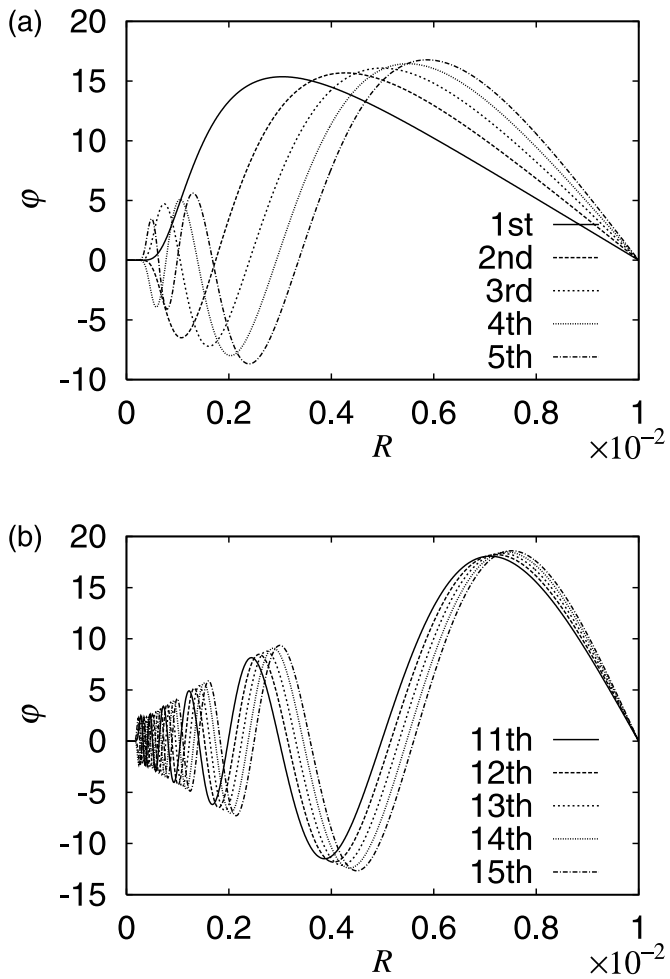

FIG. 8.—Same as Fig. 5, but for $\varepsilon = 10^{-4}$.

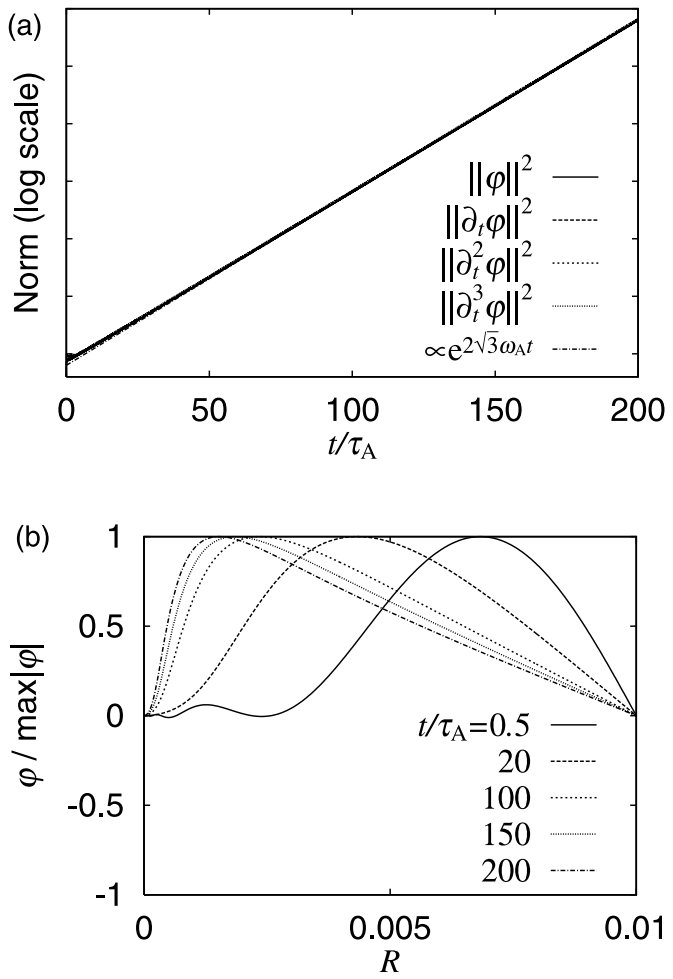

FIG. 9.—Numerical solution of the initial-value problem. (*a*) Time evolution of the norm. The lines almost overlap. (*b*) Spatial structure of the perturbation (normalized). Even though the norm grows exponentially, the spatial structure continues to change slowly.

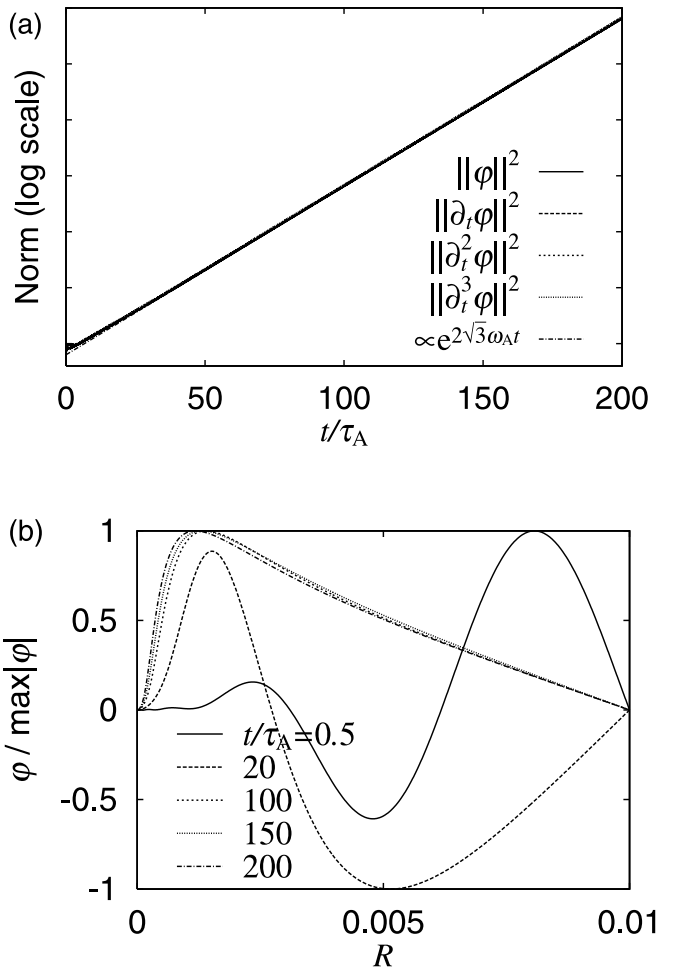

FIG. 10.—Same as Fig. 9, but for a different initial condition.

small but finite R if ω^2 is close to $-3\omega_A^2$. The computational domain is chosen to be from $R = 0$ to $R = R_a = 0.01$, and 1000 grid points are used. It should be important to note that the eigenvalues do not change for $\varepsilon \neq 0$ when the number of grid points is changed. This means the eigenvalues obtained numerically here are discrete. In contrast, for $\varepsilon = 0$, the eigenvalues become closer to $\omega^2 = -3\omega_A^2$ as the number of grid points becomes larger. Thus, these eigenvalues should be a numerically discretized continuum. In addition, the eigenfunctions for the smallest eigenvalues are also shown in Figure 7. As ε decreases, the peak of φ approaches its value for the Keplerian rotation. It is noted that those eigenfunctions are normalized by their norms. Figure 8 shows the eigenfunctions for $\varepsilon = 10^{-4}$ belonging to (Fig. 8*a*) the first to the fifth smallest eigenvalues and (Fig. 8*b*) the 11th to the 15th smallest eigenvalues. We see rapid oscillation in R, which is similar to the eigenfunctions for $\varepsilon = 0$; however, the rapid oscillation disappears near the origin. The range of this disappearance becomes narrower as ε becomes smaller.

Next, we show the numerical solution to the initial-value problem in equation (22) for the same computational domain. The wavenumber was chosen as $k = 1$. Similar to the eigenvalue approach, ξ_R is changed to φ. The number of grid points in R was chosen as 1000.

Figure 9*a* shows the time evolution of the norm. The initial conditions were chosen as $\partial^2\varphi/\partial t^2 = \sin(\pi R/R_a)$ and $\varphi = \partial\varphi/\partial t = \partial^3\varphi/\partial t^3 = 0$. We see that the norm oscillates at the very beginning and it starts to grow as approximately $\exp(2\sqrt{3}\omega_A t)$. As a reference, a function proportional to $\exp(2\sqrt{3}\omega_A t)$ is also plotted. Thus, the growth rate of φ is approximately $\sqrt{3}\omega_A$, which agrees well with the smallest eigenvalue $\omega^2 = -2.9997\omega_A^2$ in the eigenvalue approach.

Figure 9*b* shows the time evolution of the initial perturbation. At $t = 20\tau_A$ the norm grows as $\exp(2\sqrt{3}\omega_A t)$, and we may recognize that the instability is in the linearly growing phase. However, we find that the spatial structure of the perturbation continues to change slowly in the "linearly growing phase." The peak of the mode moves toward $R = 0$. This phenomenon is expected from the analysis via the Laplace transform. Since the poles are distributed densely, the most unstable mode needs a significantly long time to dominate the others.

Figure 10 shows the time evolution of the norm and the spatial structure of the perturbation for another set of initial conditions, $\partial^2\varphi/\partial t^2 = \exp(-R/R_a)\sin(3\pi R/R_a)$ and $\varphi = \partial\varphi/\partial t = \partial^3\varphi/\partial t^3 = 0$. The wavenumber was chosen as $k = 1$. The norm grows as $\exp(2\sqrt{3}\omega_A t)$ again while it oscillates in the beginning. The growth rate of the norm is determined by the smallest eigenvalue in the eigenvalue approach and does not depend on the initial condition. However, we see an interesting phenomenon in the spatial structure of the perturbation; it is significantly different from that in Figure 9*b* at $t = 20\tau_A$, although the norm is growing exponentially with the maximum growth rate obtained by the eigenvalue approach. Therefore, we find that the time evolution of the spatial structure of the perturbation strongly

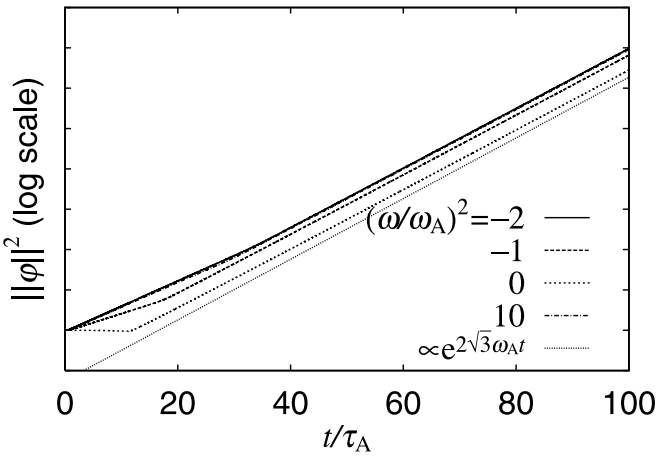

FIG. 11.—Time evolution of the norm when an eigenfunction is chosen as the initial condition. The lines for $\omega^2/\omega_A^2 = -2$ and 10 almost overlap.

depends on the initial condition even in the "exponentially growing phase." After a significantly long time, the spatial structure of the perturbation becomes similar to that in Figure 9, and the peak of the perturbation continues to move slowly toward $R = 0$.

Finally, we show the time evolution of the norm in Figure 11 taking the initial form of φ as an eigenfunction and $\partial\varphi/\partial t = \partial^2\varphi/\partial t^2 = \partial^3\varphi/\partial t^3 = 0$. The wavenumber was chosen as $k = 1$. For example, if we choose the eigenfunction for $\omega^2 = -\omega_A^2$ as an initial condition, the norm evolves as $\exp(2\omega_A t)$ at the beginning. However, around $t = 20\tau_A$, the growth rate of the norm changes to $2\sqrt{3}\omega_A$. Similarly, we see a sudden change in the growth rate of the norm from 0 to $2\sqrt{3}\omega_A$ if the initial condition is the eigenfunction for $\omega^2 = 0$. This could be explained by the discretizing and round-off errors. Let us suppose that we choose the eigenfunction for $\omega^2/\omega_A^2 = 0$ as an initial condition. A numerical error can be included in the last digit in the double-precision computation, and the error might include the component of the fastest eigenmode. This means that the magnitude of the fastest eigenmode is approximately 10^{-16} smaller than the "real" perturbation we are interested in. The real perturbation does not grow; however, the error component grows with its growth rate $\sqrt{3}\omega_A$. Then the magnitude of the error can reach the order of unity after time $t/\tau_A \simeq \ln 10^{16}/\sqrt{3} \simeq 21$. This seems to be of the same order as the value observed in Figure 11. It should be noted, however, that this estimate does not necessarily deny that the observed phenomena come from the nonorthogonality of the eigenfunctions in the non-Hermitian system.

If we choose the eigenfunction corresponding to the stable mode ($\omega^2 > 0$) as the initial condition, the norm grows exponentially in Figure 11. The growth rate is approximately $2(1.78)^{1/2}\omega_A$. As pointed out in § 3, two values of ω^2 give the same potential V, and the stable and the unstable modes can share an eigenfunction. The pair of roots $\omega^2 = 10\omega_A^2$ and $-1.78\omega_A^2$ have a common eigenfunction whose norm has a growth rate of $2(1.78)^{1/2}\omega_A$.

6. CONCLUSIONS

We have studied the linear stability of a Keplerian disk against the magnetorotational instability (MRI), whose time evolution is governed by a non-Hermitian operator. The axisymmetry of the mode especially simplifies the eigenvalue equation, and it superficially looks like the Schrödinger equation. However, the irregular singularity at the center of the disk due to the Keplerian rotation cooperates with the intrinsic non-Hermitian property of the system to generate the continuum of eigenvalues in both stable (purely oscillating) and unstable (exponentially growing) regimes. All the eigenfunctions are square integrable, vanish at the center, have rapid radial variation near the center of the disk, and satisfy the boundary condition there intrinsically. In our analysis, the small-radius ($R \ll 1$ or $R \ll R_0$ in the physical dimension) approximation is used, and a suitable choice of R_0 can extend the region of the instability throughout the disk. Although this eigenvalue approach gives us particular solutions to the evolution equation, we must interpret the results carefully, since not only is the number of eigenfunctions too large, but they are also not orthogonal to each other. Thus, we have analyzed the time evolution of the MRI via the Laplace transform as well as the numerical simulations. The maximum growth rate differs significantly from its value found from the local analysis. We have found that the spatial structure of the perturbation continues to change even as the norm of the mode grows exponentially. This is because the poles are distributed densely on the unstable side, and therefore, the most unstable mode needs an appreciably long time to dominate the others.

The authors would like to thank S. M. Mahajan for a fruitful discussion.

APPENDIX

GENERAL ROTATION PROFILE

In § 3 we obtained the eigenfunctions for the Keplerian rotation. We can obtain the eigenfunctions for more general rotation profiles. When the equilibrium rotation frequency is given by $\Omega^2 = R^p$, the potential V becomes

$$V = \frac{3}{4}R^{-2} + k^2\left[1 - \frac{(p+4)\omega^2 - p\omega_A^2}{(\omega^2 - \omega_A^2)^2}R^p\right]. \tag{A1}$$

Thus, $p < -2$, including the Keplerian rotation ($p = -3$), yields the irregular singular point at $R = 0$. The rotation speed $R\Omega$ decreases with radius in this case. If $p \geq -2$, $R = 0$ becomes the regular singular point. Then the conventional Frobenius series solution can be constructed. In this appendix we concentrate on $p < -2$ or the irregular singular point.

In the region with $R \ll 1$, the R^p term becomes dominant, and then the eigenvalue problem can be written as

$$R^{-p}\frac{d^2\varphi}{dR^2} + \lambda_p\varphi = 0, \tag{A2}$$

where λ_p is given by

$$\lambda_p = k^2 \frac{(p+4)\omega^2 - p\omega_A^2}{(\omega^2 - \omega_A^2)^2} = \text{const.} \tag{A3}$$

By transforming the coordinate as $x = R^{(p+2)/2}$, we find the solution analytically for $\lambda_p > 0$ as

$$\varphi = c_1 R^{1/2} J_{1/|p+2|}\left(\frac{2\lambda_p^{1/2}}{|p+2|} R^{(p+2)/2}\right) + c_2 R^{1/2} Y_{1/|p+2|}\left(\frac{2\lambda_p^{1/2}}{|p+2|} R^{(p+2)/2}\right). \tag{A4}$$

Both of the eigenfunctions go to zero as R goes to zero. The eigenfunctions are square integrable as

$$\int_0^{R_a} dR\, R|\xi_R|^2 = \frac{-2}{2+p} \int_{R_a^{(2+p)/2}}^{\infty} dx\, x^{(2-p)/(2+p)} \left| c_1 J_1\left(2\sqrt{\lambda_p} x\right) + c_2 Y_1\left(2\sqrt{\lambda_p} x\right) \right|^2. \tag{A5}$$

REFERENCES

Balbus, S. A., & Hawley, J. F. 1991, ApJ, 376, 214
———. 1998, Rev. Mod. Phys., 70, 1
Bondeson, A., Iacono, R., & Bhattacharjee, A. 1987, Phys. Fluids, 30, 2167
Chandrasekhar, S. 1960, Proc. Natl. Acad. Sci., 46, 253
Chini, R., et al. 2004, Nature, 429, 155
Curry, C., Pudritz, R. E., & Sutherland, P. G. 1994, ApJ, 434, 206
Dubrulle, B., & Knobloch, E. 1993, A&A, 274, 667
Frieman, E., & Rotenberg, M. 1960, Rev. Mod. Phys., 32, 898
Furukawa, M., & Tokuda, S. 2005, Phys. Rev. Lett., 94, 5001
Hirota, M., Tatsuno, T., & Yoshida, Z. 2005, Phys. Plasmas, 12, 2107
Keppens, R., Casse, F., & Goedbloed, J. P. 2002, ApJ, 569, L121
Tatsuno, T., Volponi, F., & Yoshida, Z. 2001, Phys. Plasmas, 8, 399
Velikhov, E. P. 1959, Soviet Phys.-JETP, 36, 995